Kinetic coupling of the respiratory chain with ATP synthase, but not proton gradients, drives ATP production in cristae membranes

Alexandra Toth[a], Axel Meyrat[b], Stefan Stoldt[c], Ricardo Santiago[a], Dirk Wenzel[d], Stefan Jakobs[c,e], Christoph von Ballmoos[b,1], and Martin Ott[a,1]

[a]Center for Biomembrane Research, Department of Biochemistry and Biophysics, Stockholm University, SE-106 91 Stockholm, Sweden; [b]Department of Chemistry and Biochemistry, University of Bern, CH-3012 Bern, Switzerland; [c]Department of NanoBiophotonics, Max Planck Institute for Biophysical Chemistry, DE-37077 Göttingen, Germany; [d]Laboratory of Electron Microscopy, Max Planck Institute for Biophysical Chemistry, DE-37077 Göttingen, Germany; and [e]Clinic of Neurology, University Medical Center Göttingen, DE-37075 Göttingen, Germany

Edited by Jodi Nunnari, University of California, Davis, CA, and approved December 19, 2019 (received for review October 22, 2019)

Mitochondria have a characteristic ultrastructure with invaginations of the inner membrane called cristae that contain the protein complexes of the oxidative phosphorylation system. How this particular morphology of the respiratory membrane impacts energy conversion is currently unknown. One proposed role of cristae formation is to facilitate the establishment of local proton gradients to fuel ATP synthesis. Here, we determined the local pH values at defined sublocations within mitochondria of respiring yeast cells by fusing a pH-sensitive GFP to proteins residing in different mitochondrial subcompartments. Only a small proton gradient was detected over the inner membrane in wild type or cristae-lacking cells. Conversely, the obtained pH values did barely permit ATP synthesis in a reconstituted system containing purified yeast F_1F_0 ATP synthase, although, thermodynamically, a sufficiently high driving force was applied. At higher driving forces, where robust ATP synthesis was observed, a *P*-side pH value of 6 increased the ATP synthesis rate 3-fold compared to pH 7. In contrast, when ATP synthase was coreconstituted with an active proton-translocating cytochrome oxidase, ATP synthesis readily occurred at the measured, physiological pH values. Our study thus reveals that the morphology of the inner membrane does not influence the subcompartmental pH values and is not necessary for robust oxidative phosphorylation in mitochondria. Instead, it is likely that the dense packing of the oxidative phosphorylation complexes in the cristae membranes assists kinetic coupling between proton pumping and ATP synthesis.

mitochondria | ATP synthesis | cristae | energy conversion | kinetic coupling

Mitochondria are the central organelles for cellular energy conversion, hosting the complexes of the respiratory chain and the rotary F_1F_0 ATP synthase to drive ATP synthesis through oxidative phosphorylation (OXPHOS). The complexes of the respiratory chain translocate protons from the mitochondrial matrix into the intermembrane space, thereby creating an electrochemical proton gradient across the inner membrane, which drives transport processes over the inner membrane as well as ATP synthesis. Mitochondria have a particular ultrastructure where an outer membrane encloses the inner membrane, which in turn folds into invaginations termed cristae (1). This establishes subcompartments in the inner membrane with specific composition and functions. For example, protein import from the cytoplasm into the mitochondrial matrix involves the transport of fully unfolded precursor proteins through the translocases of the outer membrane (TOM complex) and the inner membrane (TIM23 complex) (2, 3). Consequently, TOM and TIM23 cooperate and interact physically to form large assemblies connecting both membranes (4). This positions the TIM23 in the inner boundary membrane (IBM) (5, 6) that opposes the outer membrane. Furthermore, the early steps in the assembly of complex III and complex IV occur preferentially in this membrane (7). On the contrary, the oxidative phosphorylation machinery and assembly of the F_1F_0 ATP synthase is strongly enriched in the cristae membranes (5–9), and this membrane compartment expands when cells are respiring or have a high energy demand (10). The soluble compartment inside cristae, the intracristae space (ICS), is also an important reservoir of cytochrome *c*, and a specific pathway remodels the inner membrane during apoptosis for efficient release of cytochrome *c* from mitochondria to the cytoplasm during cell death induction (11).

The physiological role of cristae membranes is currently not known. The recurring observation that they contain most of the OXPHOS complexes indicates that they primarily serve bioenergetic functions and, in principle, two nonexclusive hypotheses have been put forward to explain the relevance of cristae formation. First, the ICS could constitute a soluble compartment that facilitates ATP synthesis by allowing establishment of a strong transmembrane proton gradient. Electron cryotomography together with simulations suggested that the intracristae compartment could act as a proton sink analogous to the lumen

Significance

Mitochondrial energy conversion occurs in the folded invaginations of the inner mitochondrial membrane termed cristae. Electron microscopy identified these structures 75 y ago and inspired work regarding the mechanisms of mitochondrial ultrastructure formation and bioenergetics. Here we employed pH-sensitive GFP variants directed to the cristae lumen with reconstitution experiments to reveal the principal significance of cristae formation for oxidative phosphorylation. Specifically, we show that the intracristae lumen does not provide a reservoir for substrate protons for ATP synthesis. Instead, our analyses suggest that the tight packing of the oxidative phosphorylation machinery in the cristae membranes permits the kinetic coupling of proton extrusion by the respiratory chain with the proton-consuming ATP synthase.

Author contributions: A.T., A.M., S.S., S.J., C.v.B., and M.O. designed research; A.T., A.M., S.S., R.S., and D.W. performed research; A.T., A.M., S.S., D.W., S.J., C.v.B., and M.O. analyzed data; and A.T., S.S., S.J., C.v.B., and M.O. wrote the paper.

The authors declare no competing interest.

This article is a PNAS Direct Submission.

Data deposition: Data supporting this manuscript have been uploaded on the Mendeley Dataset public repository (DOI: 10.17632/6vcjtzxgmj) or are presented within this paper and in the accompanying *SI Appendix*.

[1]To whom correspondence may be addressed. Email: christoph.vonballmoos@dcb.unibe.ch or martin.ott@dbb.su.se.

This article contains supporting information online at https://www.pnas.org/lookup/suppl/doi:10.1073/pnas.1917968117/-/DCSupplemental.

First published January 21, 2020.

of thylakoids to provide substrate protons for ATP synthesis (12–14). Consequently, a lower pH value in the ICS than in the IMS opposing the IBM is expected. However, proton concentrations or transmembrane proton gradients present in these highly confined mitochondrial subcompartments have not been comparatively determined. A second hypothesis for the occurrence of cristae is that the enrichment of the respiratory chain and ATP synthase in these membranes positions the OXPHOS complexes into close proximity. This allows producers and consumers of the proton motive force to be kinetically coupled, presumably through a mechanism commonly termed lateral membrane proton diffusion (15–18). A previous study employing a pH-sensitive GFP derivative revealed the presence of a small lateral proton gradient of ~0.3 pH units between the F_1F_0 ATP synthase (pH ~7.3) and cytochrome *c* oxidase (pH 7) in the intermembrane space of respiring HeLa cells (19). These values challenge the theory of a local proton sink, but the study used plasmid-borne overexpressed GFP fusion proteins without providing their mitochondrial sublocalization and proof of their assembly into complexes, and did not analyze transmembrane proton gradients.

In this study, we determined the local pH in actively respiring yeast cells in specific mitochondrial subcompartments. We attached the ratiometric pHGFP to the C-termini of mitochondrial proteins at their chromosomal location, ensuring expression levels close to the wild type protein. Surprisingly, our analyses revealed absence of a substantial proton gradient across the inner membrane of respiring cells. Moreover, the proton gradient was lower across the cristae membrane compared to the inner boundary membrane, demonstrating that the morphology of the inner membrane does not provide a means to concentrate substrate protons for ATP synthesis. Using purified yeast F_1F_0 ATP synthase reconstituted into liposomes, we found that the measured values of the transmembrane proton gradient in combination with a general membrane potential did barely allow ATP synthesis. However, when ATP synthase was coreconstituted with a respiratory proton pump, robust ATP synthesis was observed, indicating that kinetic coupling between proton translocation and ATP synthesis is more important for efficient OXPHOS than mitochondrial ultrastructure.

Results

Direction of a pH-Sensitive GFP to Different Mitochondrial Subcompartments. To determine the pH values of specific submitochondrial compartments in living cells, we engineered yeast strains to express fusion proteins between selected mitochondrial proteins and the ratiometric, pH-sensitive GFP variant pHluorin2 (pHGFP; Fig. 1*A*) (20, 21). To this end, selected mitochondrial proteins were genetically manipulated at their authentic chromosomal locations (22) to allow protein expression at the native levels. pHGFP was fused to the C terminus of different integral membrane proteins, exposing their C termini to the intermembrane space, namely Atp20 (subunit g) of the F_1F_0-ATP synthase, Cox7 of cytochrome *c* oxidase, and Tim23 of the TIM23 translocase. Furthermore, the soluble protein citrate synthase (Cit1) was tagged to report the pH in the mitochondrial matrix, and Tom70 from the TOM complex in the outer mitochondrial membrane was used to expose pHluorin2 to the cytosol (Fig. 1*A*). Western blotting confirmed that the GFP-fusion proteins had the expected sizes and that free GFP was absent (Fig. 1*B*). Respiratory growth capacity of these strains on the nonfermentable carbon source glycerol was not affected by the manipulations (Fig. 1*C*). Finally, two-dimensional blue native/sodium dodecylsulfate (SDS) gel electrophoresis confirmed that the dimer of ATP synthase (subunit g stabilized the F_1F_0 dimer), as well as the TIM–TOM supercomplex, were intact and contained the respective tagged subunit (Fig. 1*D*). Cox7 was partly released from the supercomplexes, possibly due to its peripheral binding to the oxidase (23–25). However, Cox7 is essential for cytochrome *c* oxidase activity and assembly, and we did not observe decreased steady-state levels of the oxidase subunit Cox2 or an impact on respiratory growth (Fig. 1 *B* and *C*). We therefore concluded that the tagged proteins were fully functional and supported OXPHOS.

Mitochondrial Sublocalization of pHGFP-Tagged Proteins. Previous studies demonstrated an enrichment of the proteins studied here in different compartments of the inner mitochondrial membrane (5–7, 9, 26, 27). To exclude that the C-terminal tagging of the proteins affected their submitochondrial localization, we determined the localization and distribution of the different proteins by fluorescence and electron microscopy techniques utilizing an antibody against GFP that detects all fusion proteins. First, distribution of the tagged proteins in whole cells was analyzed by confocal laser scanning microscopy, and, as expected, all proteins were found exclusively in mitochondria (Fig. 2 *A–E*, *Left*). Next, quantitative immunogold labeling of cryosectioned yeast cells was used to determine the distribution of the proteins in the different subcompartments. To this end, cryosections of the yeast cells were incubated with GFP-specific antibodies, which in turn were detected by protein A-gold to determine the submitochondrial localizations of the pHGFP fusion proteins (Fig. 2*B*). As expected, Tom70-pHGFP was mainly observed in close proximity to the outer membrane (Fig. 2 *C*, *Right*), and Tim23-pHGFP showed a similar distribution profile (Fig. 2 *D*, *Right*), confirming its enrichment in the IBM that opposes the outer membrane. In contrast, Cox7-pHGFP and Atp20-pHGFP were enriched in the cristae membrane (Fig. 2 *A* and *C–E*, *Right*). This enrichment is in agreement with the well-documented preferential localization of the OXPHOS system in this part of the inner membrane. We therefore concluded that the tagged proteins are localized in their natural, expected mitochondrial subcompartments.

Local pH at the Crista Membrane, Matrix, and Cytosol during Respiration. pHGFP is a pH-sensitive variant of GFP with a bimodal excitation maximum at 395 and 475 nm with a uniform emission peak at 509 nm (20). By plotting the ratio of emissions measured at excitation at 395 nm and 475 nm against a set of different pH values, a calibration curve is generated that is used to determine in vivo pH values. This method has been successfully applied previously to determine the local pH of the protein environment by fluorescence spectroscopy or microscopy (21). For this in situ calibration, cells were treated with respiratory chain inhibitors and ionophores to ensure pH equilibration of the local environments to externally applied pH conditions (Fig. 3*A*). In parallel, recombinantly expressed and purified pHGFP was incubated in buffers with the same pH values. The response of all fusion variants and the purified protein were almost identical (Fig. 3*A*), giving rise to an in situ calibration curve that was applied in the subsequent in vivo measurements.

We next determined the in situ pH in cells grown on the nonfermentable carbon source glycerol (Fig. 3*B*), which requires profound respiratory activity and ATP synthesis (Fig. 3 *C*, *Left*, and Fig. 3 *D* and *E*). Using fluorescence spectroscopy, we found that the cytosolic pH value was 7.09 ± 0.13 (reported by Tom70-pHGFP), while the pH of the mitochondrial matrix was 7.27 ± 0.09 (at Cit1-pHGFP). These values are similar to previously published data (28), validating the chosen approach. Strikingly, however, the pH values reported from the cristae-localized pH sensor were 7.13 ± 0.17 and 7.20 ± 0.10 for the cytochrome *c* oxidase and the dimeric F_1F_0 ATP synthase, respectively, and thus about 0.24 pH units more alkaline than in the inner boundary membrane, pH 6.85 ± 0.17 (Tim23-pHGFP). Hence, only a minor proton gradient ($\Delta pH \sim 0.1$) over the mitochondrial inner membrane exists in the cristae region in respiring mitochondria. Nevertheless, a ΔpH of up to ~0.4 was measured

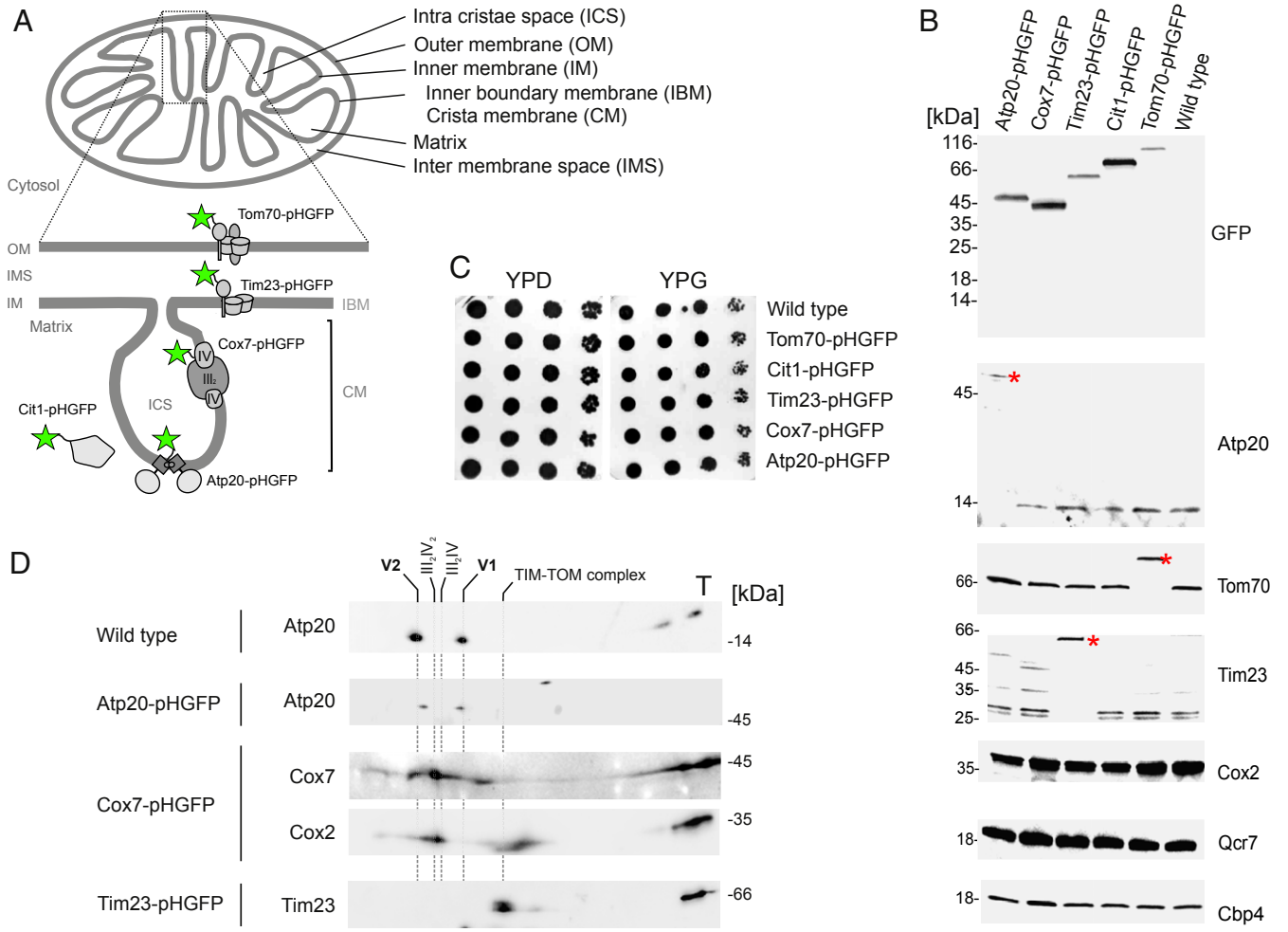

Fig. 1. Characterization of pHluorin2 fusion proteins. (*A*) Localization of the tagged proteins. (*B*) Steady-state analyses of protein accumulation. Asterisks indicate the position of the fusion protein. The levels of Cbp4 served as loading control. (*C*) Growth assay on fermentative and nonfermentative media. Cells were spotted in 10-fold serial dilutions on media containing respiratory (YPG) or fermentative (YPD) carbon sources and grown at 30 °C. (*D*) Two-dimensional blue native (BN)/SDS PAGE Western blot showing the presence of the F_1F_0 ATP synthase dimer, the supercomplexes of the respiratory chain, and the TIM–TOM supercomplex. Digitonin lysates of mitochondria from the indicated strains were first separated on BN PAGE, and the lanes excised and mounted onto SDS/PAGE. After electrophoresis, the proteins were visualized by Western blotting with the indicated antibodies.

over the matrix and the inner boundary membrane, which is close to the previously reported value of 0.5 units (29). Similar to results obtained in HeLa cells (19), we also found a little lateral pH gradient between cytochrome *c* oxidase and F_1F_0 ATP synthase. When cells were shifted to glucose fermentation (Fig. 3*B*), the pH at all fusion proteins was more alkaline by >0.6 pH units (Fig. 3 *C*, *Right*, and Fig. 3 *D* and *E*). This alkalization during fermentation has been previously observed and explained by the action of the V-type ATP synthases that are pumping protons from the cytoplasm to the vacuole. These pumps are activated upon exposure to glucose (30). The increased pH in the mitochondrial matrix is most likely due to the down-regulation of the respiratory chain activity in the presence of glucose, when the main part of ATP is generated by glycolysis and cytosolic NAD^+ is regenerated by conversion of pyruvate to ethanol (31). This results in a reduced Krebs cycle activity in mitochondria that is accompanied by a lower proton concentration in the matrix compartment (28).

In Vivo pH Measurements in Cells Lacking Normal Cristae. Because no major proton gradient was measured across the cristae membrane in wild type cells, we next asked how the proton gradient would change in strains with aberrant inner membranes. Dimerization of ATP synthase is required for cristae formation, as has been observed in mutants lacking dimer-specific subunits of ATP synthase (32–34) and in reconstitution experiments using purified ATP synthase dimers (35). Instead of tubular cristae, onion-like concentric layers of inner membrane are formed in a mutant lacking Atp20 (Fig. 4*A*). These layers of inner membrane contain the oxidative phosphorylation system and separate the matrix space into distinct compartments (34, 36). As reported previously, deletion of *ATP20* provokes decreased respiratory growth on nonfermentative media such as glycerol (37) (Fig. 4*B*). This is at least partly caused by a decrease in cytochrome *c* oxidase activity that also affects assembly of respiratory supercomplexes (Fig. 4*C*) (38). This reduction in respiratory chain activity, however, cannot be explained by a decrease in levels of the oxidative phosphorylation system (39) (Fig. 4*D*). Tagging Cox7, Tim23, Cit1, or Tom70 with pHGFP did not aggravate the slight respiratory growth defect of the *atp20Δ* cells (Fig. 4*B*). Despite the absence of cristae, no major difference of the pH values between the two strains was detected (Fig. 4*E*). A small but consistent pH increase of ~0.2 pH units was found for Cox7 of complex IV. This elevated pH (7.4) leads to a slightly inverted transmembrane proton gradient in comparison to the wild type. Inhibition of the F_1F_0 ATP synthase with oligomycin corrected

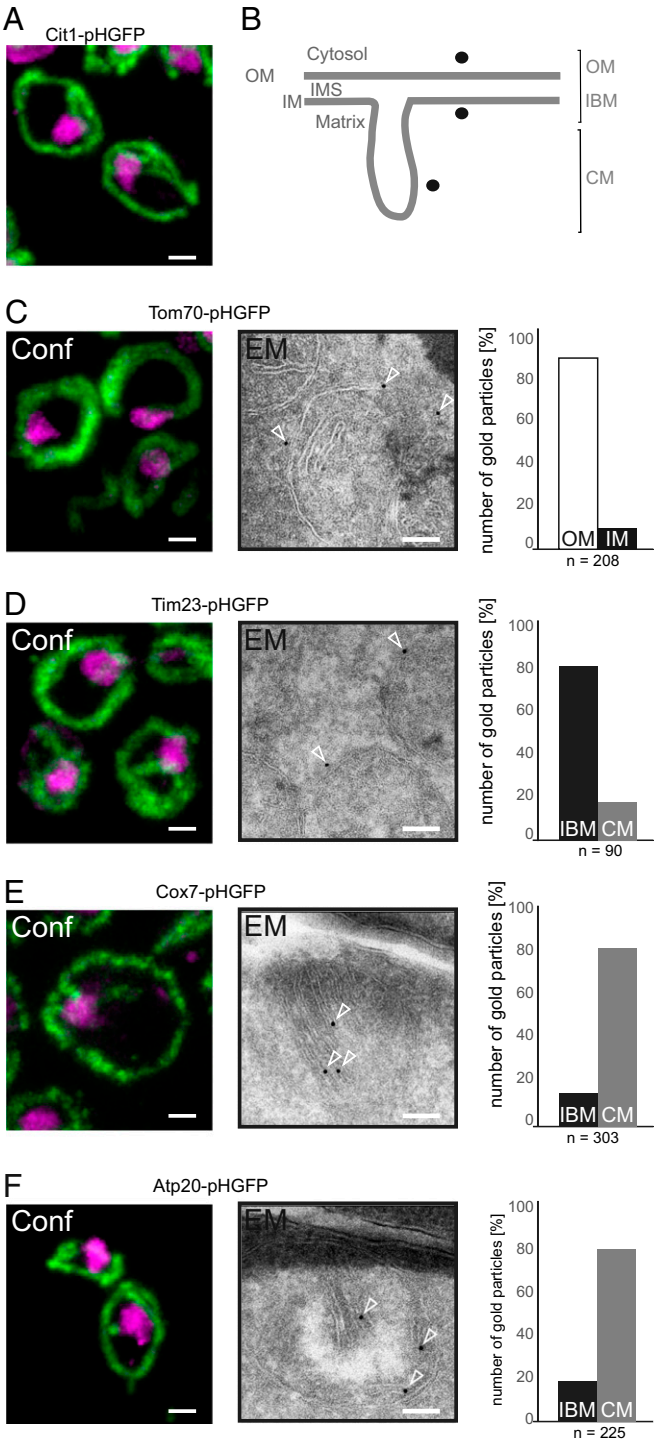

Fig. 2. Analysis of the submitochondrial distribution of pHGFP fusion proteins via confocal light (Conf; *A–F*, *Left*) and electron microscopy (EM; *B–F*, *Middle* and *Right*). Yeast cells expressing endogenously tagged Cit1-pHGFP (*A*), Tom70-pHGFP (*C*), Tim23-pHGFP (*D*), Cox7-pHGFP (*E*), and Atp20-pHGFP (*F*), respectively, were recorded using confocal immunofluorescence light microscopy. DNA was labeled using DAPI and is shown in magenta; depicted are maximum-intensity projections along the *z* axis. (*B*) Illustration of the principle of immunoelectron microscopy. Cells were labeled with a GFP-specific antibody and protein A-gold and imaged via transmission electron microscopy (*C–F*, *Middle*). Quantification of the distribution of the gold particles; *n* indicates number of analyzed gold particles (*C–F*, *Right*). (Scale bars, 1 μm in confocal images; 100 nm for EM.)

this (Fig. 4*F*), suggesting that the decreased cytochrome *c* oxidase activity in *atp20Δ* allows the establishment of a wild type pH value in these inner membrane compartments only when the proton consumer ATP synthase is inhibited.

ATP Synthesis with Purified F_1F_0 ATP Synthase Reconstituted into Proteoliposomes. In living cells, mitochondrial ATP synthesis by the F_1F_0 ATP synthase is energized by the proton motive force *pmf*, i.e., the sum of the membrane potential ($\Delta\psi$) and the proton gradient (ΔpH) generated by the respiratory complexes. These two driving forces energize proton transfer through the F_0 part of the enzyme that is coupled by a rotational mechanism to the synthesis of ATP from ADP and P_i in the F_1 part (40–43). In order to determine whether the measured pH values in the IMS (6.8 for IBM and 7.2 for ICS) and matrix (7.3) are sufficient to drive ATP synthesis in vitro, purified F_1F_0 ATP synthase from *Saccharomyces cerevisiae* was reconstituted into liposomes. In these experiments, ATP synthesis is driven by the so-called acid/base transition procedure originally described for chloroplasts (44). Acidified proteoliposomes (same pH inside and outside of proteoliposomes) are rapidly mixed with an alkaline buffer to form a pH gradient (acidic inside). Additionally, a membrane potential (positive inside) via a K^+/valinomycin diffusion potential is applied, and ATP synthesis can be followed in real time by a luciferin/luciferase reaction (Fig. 5*A* and *SI Appendix*, Fig. S1). Technically, the maximal $\Delta\psi$ that can reliably be achieved by this method is ~140 mV. While a $\Delta\psi$ of ~180 mV has been proposed to exist in mitochondria (45), the applied *pmf* is thermodynamically sufficient to support ATP synthesis in these experiments (*Discussion* and *SI Appendix*, Table S1). Due to the small volume of the liposomes, $\Delta\psi$ and thus ATP synthesis ceases quickly, and therefore initial rates are used for calculation (46, 47) (*SI Appendix*, Fig. S1).

First, we applied conditions similar to those reported earlier for the purified yeast ATP synthase (46), using a constant $\Delta\psi$ of ~140 mV and a constant acidic pH of 6.25 at the *P*-side, and varied the *pmf* by increasing the pH of the buffer (*N*-side). In these experiments, we found that a ΔpH of ≥1 is required to elicit robust ATP synthesis (Fig. 5*B*), and ATP synthesis rate increased with increasing *pmf*. At *N*-side pH values above 8, the increase in ATP synthesis rates decreased, indicating that the *N*-side pH becomes limiting, consistent with earlier studies (46). Notably, ATP synthesis did barely occur at ΔpH 0.5 (in conjunction with a $\Delta\psi$ of ~140 mV), with a *P*-side pH of 6.25 (Fig. 5*B*, black circles), and was almost undetectable at *P*-side pH values 6.75 (Fig. 5*B*, red circle) and 7.25 (Fig. 5*B*, green circle). The two latter conditions reflect the range of the *P*-side pH and *N*-side values found in the in vivo measurements described earlier. Taken together, our and previously published data (46) indicate that the aforementioned in vivo measured pH values are not optimal for ATP synthesis.

In the next series of experiments, we used a sufficiently high *pmf* for robust ATP synthesis and evaluated the importance of the absolute *P*-side pH value on the ATP synthesis rate. To this end, maintaining a $\Delta\psi$ of ~140 mV, we have varied the *P*- and *N*-side pH values in parallel to keep a constant ΔpH 1.5 and followed ATP synthesis with a total *pmf* of ~230 mV. This results in a sigmoidal dependency on the *P*-side pH (Fig. 5*C*), showing that ATP synthesis at pH 7/8.5 is ~10 to 20% compared to pH 5.5/7, albeit with the exact same total *pmf*. How can this be explained? From the data of Fig. 5*B* and earlier findings (46), we assume that ATP synthesis rate at an *N*-side pH 8.5 is about 60% compared to pH 7. This effect is thus not sufficient to explain the observed 5-fold decrease in Fig. 5*C*. Our data thus suggest an important role for the absolute pH value on the *P*-side, corresponding to the inside of the liposome. The experiments were performed with proteoliposomes of 50-nm and 200-nm diameter to ensure a sufficient number of protons available for ATP

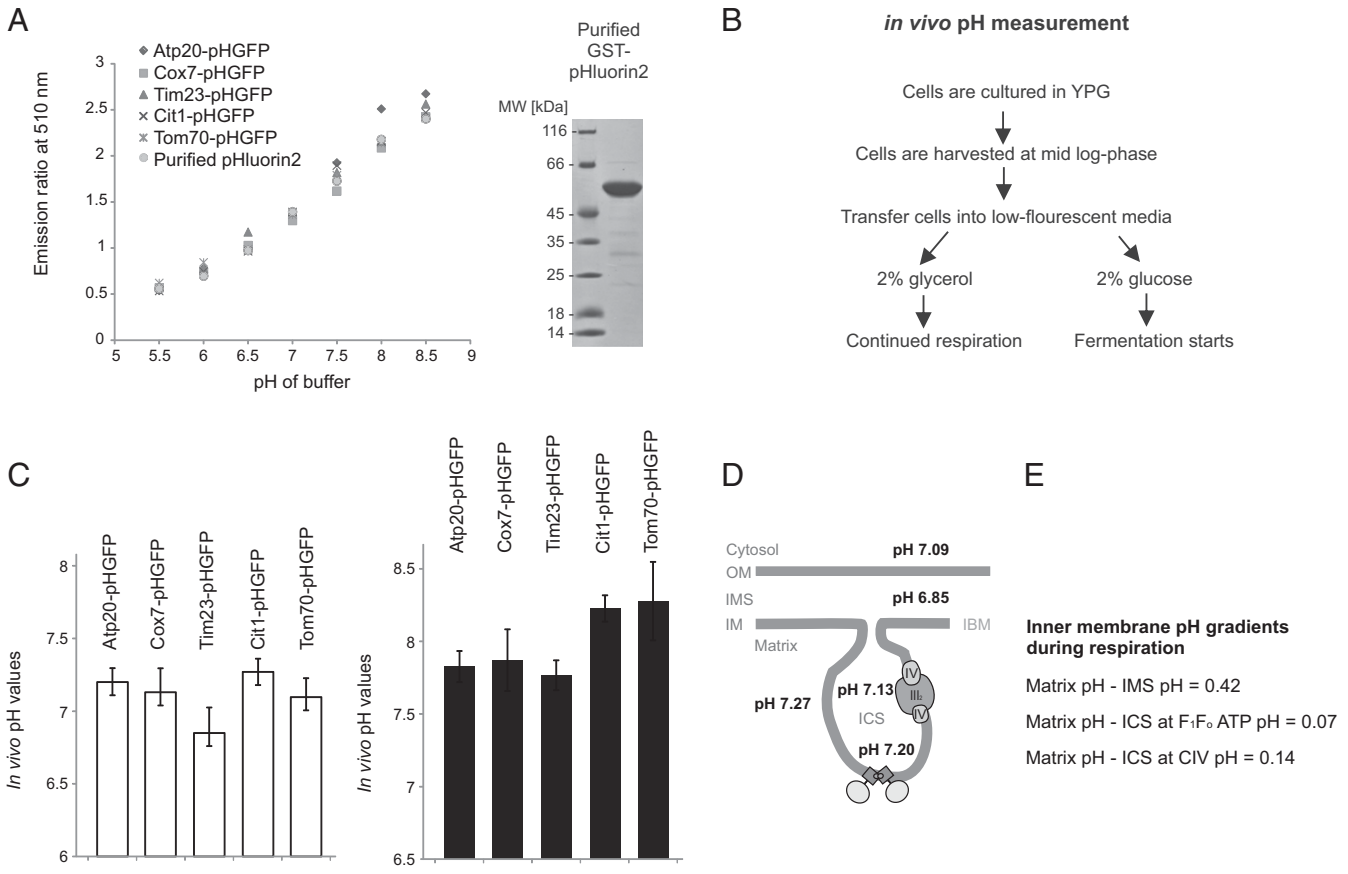

Fig. 3. Determination of pH values within mitochondria during respiration and fermentation. (*A*) In situ calibration curve for the relationship between excitation efficiency at 395 nm or 475 nm in relation to the pH. Strains were grown in media containing the respiratory carbon source glycerol, harvested, and incubated in buffers with set pH values with inhibitors and uncouplers of the respiratory chain to allow equilibration of the intracellular pH. (*Inset*) Coomassie-stained SDS PAGE with purified GST-pHGFP. (*B*) Illustration of the measurement procedure of the in vivo pH values in the cytosol, matrix, intermembrane space (IMS), and intracristae space (ICS) during respiration. (*C*) In vivo pH values during respiration (*Left*) or fermentation (*Right*). The bars represent mean values of three independent experiments with SD. (*D*) Summary with the pH gradients over the intermembrane space and the matrix, but also over matrix and the F_1F_0 ATP synthase and complex IV of the respiratory chain.

synthesis in the liposomes. As seen in Fig. 5*C*, the relative activities of the two measurements series were very similar. The small liposomes are similar in size as the ICS that has been described to be ∼30 nm wide (48).

Next, we tested the importance of the *P*-side pH with a variation of the experiment described earlier. Acid bath-driven ATP synthesis experiments were performed with a constant *pmf* of 200 mV using *P*-side pH values 6, 6.5, and 7 and a constant *P-side* pH 8, circumventing the negative effect of a high *N*-side pH. The resulting different ΔpH values (120, 90, and 60 mV) were compensated accordingly with varying Δψ values (80, 110, and 140 mV) to yield an identical *pmf* of 200 mV (exact conditions provided in *SI Appendix*, Table S1). As depicted in *SI Appendix*, Fig. S2, the same trend was observed, as ATP synthesis was ∼2.5-fold decreased at a *P*-side pH of 7 compared to pH 6, a finding fully consistent with the results in Fig. 5*C*. A molecular mechanism for the requirement of an acidic *P*-side can be proposed based on the asymmetric ion access half channels to the c-ring binding side from the *P*- and *N*-side of the membrane, as it has been measured for the Na^+-translocating ATP synthase from *Ilyobacter tataricus* and *Escherichia coli* (40, 47). The recent high-resolution structure of ATP synthases from yeast, chloroplast, and bacteria show a conserved arrangement of horizontal helices of subunit a and the c-ring in the proton translocating F_0 moiety, which is in accordance with asymmetric access channels (49–51). The data thus strongly suggest that, despite favorable thermodynamic conditions, an IMS or cristae pH value of ≤6.5 significantly increases ATP synthesis rates. Still, such a low IMS pH value was not measured in this work and has not been reported earlier for mitochondria.

However, the acid/base experiment does not mimic the physiological conditions found in respiring bacteria or mitochondria. In these, the *pmf* is established and maintained by electron-coupled proton transfer reactions of the respiratory chain. In order to test the pH requirements for robust ATP synthesis under these conditions, we have mimicked the last step of oxidative phosphorylation and coreconstituted the yeast F_1F_0 ATP synthase with the cytochrome bo_3 oxidase from *E. coli* into liposomes (52) (Fig. 5*D*). In this experimental system, electrons supplied from the outside initiate proton pumping by the bo_3 oxidase into the liposomes, establishing and continuously maintaining a *pmf* across the liposomal membrane that drives ATP synthesis (Fig. 5*E*). In contrast to the acid/base procedure, respiratory-driven ATP synthesis occurs continuously, as long as the substrates for the different enzymes are present in sufficient concentrations. To this end, proteoliposomes containing ATP synthase and bo_3 oxidase were equilibrated in buffers with different pH values ranging from 6.75 to 8.75, and ATP synthesis was initiated by proton pumping of the bo_3 oxidase. As depicted in Fig. 5*F*, at all tested pH values, robust ATP synthesis was observed. The optimal pH range was found to be between 7.25 and 7.75, while, at pH 6.75 and pH 8.75, the rates are 40% and

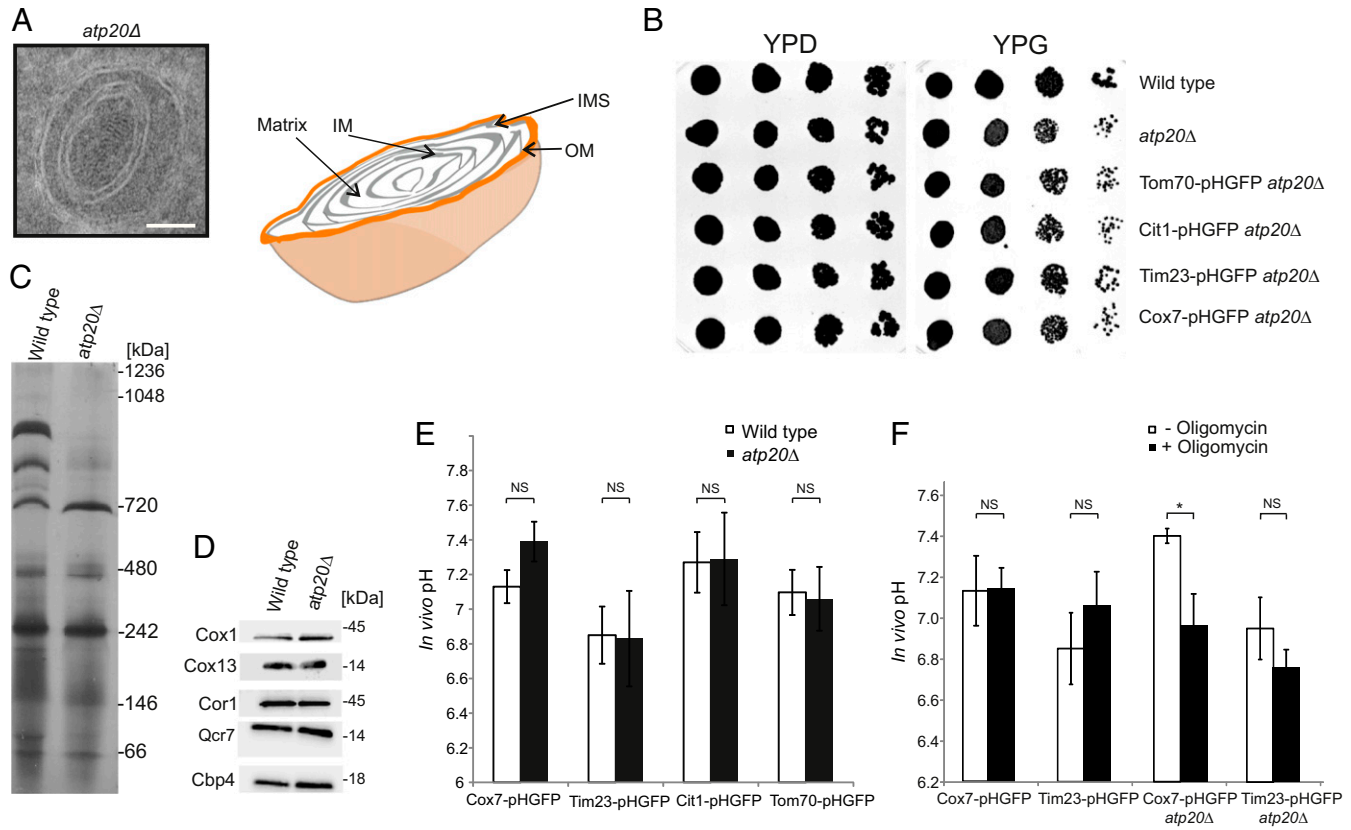

Fig. 4. Measurement of pH values in mitochondria lacking normal cristae morphology. (*A*) Transmission electron microscopy image of the *atp20Δ* strain and graphical depiction of its submitochondrial structure. The inner membrane does not contain cristae, but is folded into large concentric rings. IM, inner membrane, illustrated with gray color; OM, outer membrane, seen in orange; IMS, intermembrane space. The matrix space (white) is between the gray IM layers. (Scale bar, 100 nm.) (*B*) Growth assay of *atp20Δ* cells tagged with pHGFP on fermentative (YPD) or respiratory media (YPG). (*C*) Blue native gel, with lysed mitochondrial samples, from the wild type and *atp20Δ* strains. The F_1F_0 ATP synthase dimer was absent from the *atp20Δ* strain, and the levels of the respiratory supercomplexes (III_1IV_2) and (III_2IV_2) were reduced compared to the wild type. (*D*) Western blot of whole cell extracts of wild type and the *atp20Δ* strain. (*E*) In vivo pH values compared between the pHGFP strains and in strains lacking Atp20. (*F*) Cells were treated with the ATP synthase inhibitor or mock-treated followed by pH determination. The bars in both *E* and *F* represent mean values of three independent experiments with SD. $*P < 0.05$; NS, not significant.

~60%, respectively. This mild pH dependence is likely dictated by the F_1 moiety at lower pH and by the availability of phosphate for the ATP synthesis reaction at high pH values (46). Most importantly, in contrast to the acid/base measurements, the coreconstituted system enables optimal ATP synthesis in the measured physiological pH range of ICS and matrix. ATP synthesis occurred without any delay, demonstrating that no large ΔpH has to be built up (shown for pH 8.75; *SI Appendix*, Fig. S3).

Taken together, the acid/base measurements demonstrate that, in the absence of a proton pump, lower *P*-side pH values increase ATP synthesis rates 3-fold at identical *pmf*, and the coreconstitution experiments indicate that such low pH values are likely reached by a short-lived acidification by the proton pumping bo_3 oxidase. These data thus strongly support a scenario in which proton pumping and ATP synthesis are kinetically coupled by proximity in the membrane, as likely occurs in the mitochondrial cristae.

Discussion

Mitochondria, the prime site of cellular energy conversion, have a highly complex inner membrane architecture; invagination of the inner mitochondrial membrane creates cristae, a distinct membranous subcompartment. The enrichment of the mitochondrial OXPHOS system in the cristae membranes points to a specific function of these membranes for bioenergetics. In this system, the proton pumping complexes of the respiratory chain produce and maintain an electrochemical proton gradient across the membrane that energizes ATP production by the F_1F_0 ATP synthase. Recent electron tomography studies of intact mitochondria have further revealed that respiratory enzymes exist as supercomplexes residing in the flat regions of the cristae, while ATP synthases exist as dimers forming long rows that bend the membrane and are located exclusively at the rim of the cristae (53). Based on these findings and calculations, it was suggested that the cristae could assist in the formation of a locally increased transmembrane proton gradient (14). A specialized inner membrane architecture is also found in chloroplasts, which are similar to mitochondria, the result of an endosymbiotic event. In chloroplasts, the thylakoids constitute a closed membrane system (54), which allows the establishment of a substantial pH gradient over the membrane (12). On the contrary, cristae membranes are continuous with the inner boundary membrane through the cristae junctions, thereby connecting the ICS to the intermembrane space.

Here, by employing a pH-sensitive GFP variant, we determined the local pH values at all mitochondrial subcompartments, namely the matrix, the intermembrane space, and the intracristae space. Measurements in respiring yeast cells confirmed earlier findings of the pH values in the matrix (~7.3) and the intermembrane space (~6.8). Surprisingly, however, the pH measured in the intracristae space was ~7.2 and thus more alkaline than in the intermembrane space. We did thus not detect

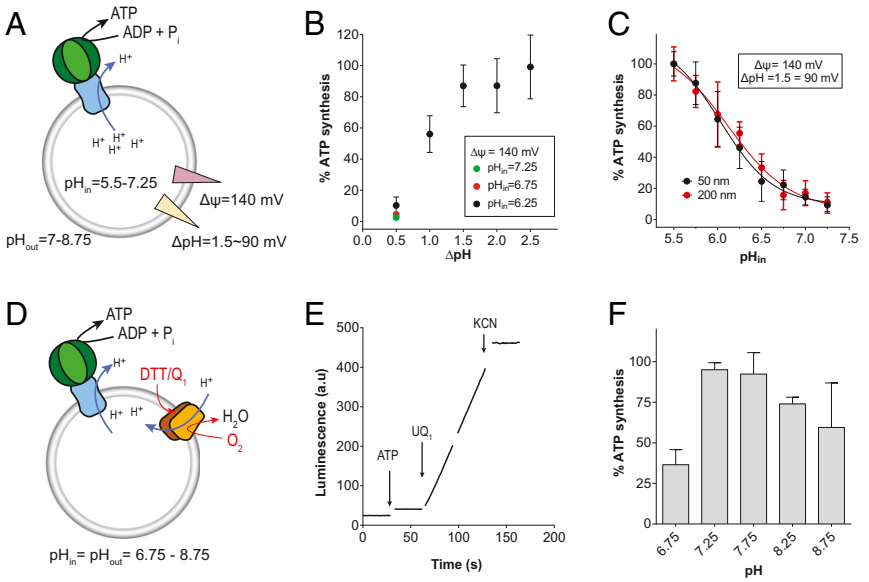

Fig. 5. Kinetic coupling between oxidative phosphorylation enzymes is essential to fuel the process. (*A*) Cartoon of the experimental setup for in vitro ATP synthesis measurements by acid bath treatment. In these experiments, in addition to ΔpH, a Δψ was established by K^+/valinomycin diffusion potential. The ATP synthesis reaction is started by rapidly mixing the acidified liposomes with alkaline buffer and detected by the luciferin/luciferase system. Further details are provided in the text. (*B*) Influence of the ΔpH on the initial rate of ATP synthesis. With a constant pH_{in} of 6.25, pH_{out} was varied between 6.75 and 8.75 (black circles). Additionally, ΔpH 0.5 was also measured with pH_{in} values of 6.75 (red circle) and 7.25 (green circle). Here, error bars are omitted for clarity (n = 3 different liposome preparations with technical duplicates). (*C*) Influence of pH_{in} on the initial rate of ATP synthesis. pH_{in} and pH_{out} were varied in parallel from 5.5 to 7.25 and 7.25 and 8.75, respectively, to establish a constant ΔpH of 1.5 (~90 mV). In addition, a Δψ of 140 mV was present, yielding a total *pmf* of 230 mV. Shown are the data for liposomes with 50-nm (black) and 200-nm (red) diameter (n = 3 different liposome preparations with technical duplicates). (*D*) Cartoon showing the experimental setup of in vitro ATP synthesis experiments in liposomes containing coreconstituted F_1F_0 ATP synthase from *S. cerevisiae* and bo_3 oxidase from *E. coli*. The reaction was started by the addition of dithiothreitol (DTT) and ubiquinol (Q_1), and ATP formation was detected by the luciferin/luciferase system. (*E*) Raw trace from a typical experiment with respiratory enzyme-driven ATP synthesis as described in *D*. Indicated by arrows are the additions of 10 to 50 nmol ATP for normalization, 20 μM ubiquinone Q_1 to start the reaction, and 500 nM potassium cyanide (KCN) to block proton pumping by bo_3 oxidase. (*F*) ATP synthesis rates of coreconstituted ATP synthase and bo_3 oxidase at different pH values. Liposomes containing the proteins were incubated in the desired buffer for 60 min, and ATP synthesis was initiated by addition of ubiquinone 20 μM Q_1 (n = 3 different liposome preparations).

a substantial transmembrane gradient across cristae membranes. When the same experiments were performed in an *atp20Δ* strain, where the inner membranes are found as concentric layers and cristae structures are absent, the pH values at the different enzyme location were essentially unchanged compared to the wild type. Notably, two small differences were observed. First, in comparison to the wt, Cox7-pHGFP reported a slightly higher (by ~0.2) pH that can be explained by the reduced cytochrome *c* oxidase activity in this strain. Nevertheless, *atp20Δ* cells are capable of oxidative phosphorylation, reinforcing the necessity of a local proton coupling between the respiratory chain and ATP synthase. Second, when oligomycin was added to inhibit ATP synthase, the ICS pH dropped by ~0.4 pH units in *atp20Δ* cells, a change that was not observed in wt cells. A possible explanation is that the inner membrane architecture of *atp20Δ* cells has an aberrant connectivity to the IMS that prevents normal proton flux, which allows the observation of an acidification in the ICS that is invisible in cells with normal cristae. The previously observed lateral pH gradient in mitochondria from HeLa cells between complex IV (pH ~7) and ATP synthase (pH ~7.3) was negligible in our measurements. A possible explanation for this discrepancy could be either (*i*) the use of a different pHluorin (superecliptic vs. ratiometric), (*ii*) different subunits of the OXPHOS complexes used for pHluorin fusion (subunit e vs. g in the ATP synthase, and Cox8a vs. Cox7 for cytochrome *c* oxidase), (*iii*) the use of plasmid-borne expression vs. chromosomally encoded fusion protein, or (*iv*) related to differences between the species considered. However, both studies are in line with the absence of a locally acidified environment within the intermembrane space found in wild type cristae or the concentric layers of inner membrane in the *atp20Δ* strain. Consequently, these experiments indicate the absence of a substantial proton gradient over the inner membrane in either system.

These findings do not contradict classical thermodynamics. Assuming a Δψ of 160 to 180 mV and a ΔpH of 0.1 to 0.5, the pmf in yeast is sufficiently large to thermodynamically allow ATP synthesis (55). The phosphorylation potential is given by $\Delta G_P = \Delta G_0' + RT \times \ln([ATP]/[ADP][P_i])$, where $\Delta G_0'$ is the standard potential at a given pH (55). For respiring yeast at pH 7, a $\Delta G_0'$ of ~30 kJ/mol, an ATP/ADP ratio of ~5 (56), and a [Pi] of 3 mM can be assumed, yielding a ΔG_P of ~48 kJ/mol. Using $\Delta p\,(mV) = \Delta G_P/F$, where F is the Faraday constant (0.096 $kJ \cdot mol^{-1} mV^{-1}$), this is equivalent to a total proton motive force of ~500 mV. As the ATP synthase has a 3-fold and 10-fold symmetry in the F_1 and the F_0 parts, respectively, a pmf of 500/(10/3) ≈ 150 mV is required to thermodynamically allow ATP synthesis, which is present in yeast as stated earlier. However, it is important to note that thermodynamic considerations are not suitable to predict if a reaction takes place or to draw any conclusion about the rate of the reaction.

In our in vitro measurements, we failed to observe robust ATP synthesis at the measured pH values (pH_{in} ~6.75 to 7.25 and pH_{out} ~7.25 to 7.75) and a Δψ of ~140 mV. This is surprising, as the thermodynamic energy requirements are significantly lower for ATP synthesis in proteoliposomes, as the ATP/ADP ratio in our in vitro experiments was <0.05 and $[P_i]$ is ~10 mM. Using the formula above yields a ΔG_P of ~35 kJ/mol, being equivalent to a *pmf* of 113 mV. However, in a recent study from Peterson et al., a minimal *pmf* of ~150 mV was required to shift the equilibrium from ATP hydrolysis to ATP synthesis (57). In our experiments, we have either used a total *pmf* of 230 mV (Fig. 5*C*) or 200 mV

(*SI Appendix*, Fig. S2), ensuring sufficient driving force. We find that, despite a constant *pmf*, ATP synthesis is 3 to 5 times faster at a *P*-side pH 6 compared to pH 7. During ATP synthesis, protons are pumped from the *P*-side to the *N*-side of the liposomes, and thus a sufficient number of protons have to be present within the liposomes for transport through the F_0 part. We have therefore also performed the experiments with 200-nm liposomes that offer a 64-fold larger volume compared to the 50-nm liposomes. Both series resulted in very similar results, indicating that enough protons for F_0 transport were available within the liposomes. This is consistent with liposome measurements of reconstituted F_0 parts of *E. coli* (58), spinach chloroplasts (59), or membrane vesicles of *Rhodobacter capsulatus* (60), where high proton efflux rates of >1,000 H^+s^{-1} per liposome at pH 7 or higher have been measured. In our measurements, <20 H^+ (or 6 ATP produced) are consumed within the time range that has been used to calculate the initial rates. Here, both experiments in Fig. 5*C* and *SI Appendix*, Fig. S2 show the same trend, but one should be careful to quantitatively compare the two results. While, in Fig. 5*C*, the *pmf* was kept constant by only varying pH_{in} and pH_{out} in parallel, in *SI Appendix*, Fig. S2, pH_{out} was kept constant and the changing ΔpH was compensated by varying Δψ values. This leads to many different experimental conditions that can affect an exact quantitative outcome (the detailed conditions of all experiments are provided in *SI Appendix*, Table). Furthermore, in contrast to the *E. coli* ATP synthase (47), the yeast enzyme seems to be slowed by pH_{out} values above pH 8, further complicating an exact quantitative analysis. Nevertheless, both experiments show effects larger than 3-fold between pH 6 and 7. Interestingly, this effect is lost when the ATP synthase is coreconstituted together with a redox-driven proton pump that establishes and maintains a *pmf* across the liposomal membrane, similar to what is found in the mitochondria by respiratory complexes I to IV. Here, the rate of ATP synthesis is essentially constant between pH 7.25 and 8.25, while the lower rates at 6.75 and 8.75 are due to effects of the F_1 part. Such a discrepancy between static (acid-bath experiment) and dynamic *pmf* formation (primary pump) has also been reported for ATP synthesis in *E. coli* (47) and in the alkaliphilic bacteria *Bacillus* OF4 (61). In the latter, the ΔpH is even inverted (more alkaline on the *P*-side than on the *N*-side), and the resulting *pmf* (<100 mV at pH 10) is very low, but, nevertheless, oxidative phosphorylation-driven growth is supported.

A possible molecular explanation for this conundrum has been suggested by a hypothesis known as lateral proton transfer along the membrane surface. This hypothesis proposes that protons ejected by proton pumping enzymes are not immediately released into the bulk, but rather stay close to the membrane surface, along which they can travel in a two-dimensional manner. Consequently, nearby localized proton consumers (e.g., ATP synthase) can exploit these protons before they are equilibrated with the bulk. The exact molecular mechanisms for such a kinetic proton trap, in which lipid head groups, protein side chains, and water–water interactions are proposed, are currently debated (15, 17, 62–66). Our data therefore indicate that, indeed, a kinetic proton coupling between the proton pump and the ATP synthase supports oxidative phosphorylation in the liposomes and consequently in mitochondrial cristae. Taken together, our data suggest that the mitochondrial ultrastructure does not contribute to the establishment of local pH gradients. In contrast, the organization of the OXPHOS systems in cristae membranes provides an optimal environment for kinetic proton coupling between the respiratory chain and the ATP synthase. This is supported by recent experiments with coreconstituted enzyme from *E. coli*, which have indicated that the protein density of these enzymes within the lipid membrane is a crucial parameter for the effectiveness of the kinetic coupling (64, 67). It will be important to test whether the general concept of cristae organization to support kinetic coupling also applies to animal mitochondria, which have an ATP synthase with fewer c-subunits than yeast and display a great variety of inner membrane architecture.

Materials and Methods

Yeast Strains and Cloning. Strains used in this study were isogenic to BY4741 (MATa *his3Δ1 leu2Δ0 met15Δ0 ura3Δ0*) or W303a (MATa *leu2-3,112 trp1-1 can1-100 ura3-1 ade2-1 his3-11,15*). The plasmid encoding the enhanced ratiometric pHluorin2 (pHGFP) was a gift from Mari Valkonen (VTT Technical Research Center, Espoo, Finland). The coding sequence of pHGFP was PCR-amplified and cloned into the pYM28 with SalI and BamHI to allow C-terminal tagging of target proteins (68). Yeast cells were transformed with PCR products (69) encompassing the pHluorin2 sequences and the selection cassette *mxHIS3*. A PCR product harboring the *atp20::kanMX4* gene was used to transform yeast strains expressing pHGFP fusion proteins. Positive transformants were selected on agar plates containing geneticin sulfate (G418 200 μg/mL final; Roth). Ratiometric pHGFP was cloned with SalI and BamHI into the expression vector pGEX-4T-1 to allow purification of the protein as a GST fusion.

In Situ Calibration of pHGFP Strains, In Vivo pH Measurement, and the Influence of Respiratory Uncouplers on *atp20Δ* Strains. Cells were inoculated in 50 mL of YPG (yeast peptone, 2% glycerol) and grown for 16 h at 30 °C. The cultures were then diluted to early log phase and let grow for 2 h at 30 °C. The cells were harvested at midlog phase (OD 0.3 to 0.5) at 3,000 × *g* for 5 min at RT. In situ calibration of the yeast cells and the purified pHGFP were performed in a 96-microplate well plate (Nunc, optical bottom black; ThermoScientific) in triplicates in a Gemini EM microplate reader (SpectraMax). The amount of the calibration buffer was, in total, 150 μL for the in situ calibration. The in situ calibration buffer contained the following: 50 mM MES buffer (pH 5.5, 6.0, and 6.5), 50 mM Hepes-KOH buffer (pH 7.0 to 7.5), 50 mM Tris·HCl (pH 8.0 to 8.5), 0.2 M ammonium, acetate, 130 mM KCl, 50 mM NaCl, 20 mM sodium azide, 0.6 mM valinomycin, 17 μg/mL oligomycin A, and 13 μM FCCP. The cells were washed once with water and an OD of 2 of cells was transferred into each well and incubated for 30 min at RT. Cells were distributed into the microtiter plate and sedimented by gravity for 5 min at RT. The emission ratio from ex 395 nm over ex 475 nm was recorded at 30 °C and plotted against pH, and background fluorescence from wild-type cells was subtracted. For the calibration of the purified pHGFP, 10 mg/mL of purified protein was incubated with the same amounts of uncouplers and respiratory chain inhibitors as for the in situ calibration. For the in vivo pH measurement, the cells were cultivated as for the in situ calibration. Cells were exposed to oligomycin (33 μg/mL oligomycin A) for 30 min at RT with slight shaking. The obtained values were plotted with DPLOT (https://www.dplot.com/index.htm).

Immunofluorescence Labeling and Confocal Laser-Scanning Microscopy. Cells expressing pHGFP fusion proteins were grown in liquid medium (YPG) containing glycerol as the sole carbon source to the early exponential growth phase (OD600 nm = 0.4 to 0.7). For fixation, yeast cells were incubated with 3.7% formaldehyde in growth medium for 20 min at RT, harvested by centrifugation (800 × *g*, 3 min), and washed using a PBS/sorbitol solution (137 mM NaCl, 3 mM KCl, 8 mM Na_2HPO_4, 1.5 mM KH_2PO_4, 10% [wt/vol] sorbitol; pH 7). Finally, the yeast cell wall was partly removed by Zymolyase digestion (15 min, 30 °C). After additional washing with PBS/sorbitol buffer, the cells were attached to the surface of a poly-L-lysine–coated coverslip (RT, 30 min) and blocked (RT, 1 h; 2% [wt/vol] BSA; 0.1% [vol/vol] Tween 20/SDS in PBS/sorbitol) and the pHGFP fusion proteins were detected using primary rabbit antibodies against GFP (Abcam; RT, 1 h). Primary antibodies were detected using secondary goat anti-rabbit antibodies (Jackson ImmunoResearch) custom labeled with the dye Alexa Fluor 594 (Thermo Fisher Scientific; RT, 1 h). Following several washing steps in blocking solution and sorbitol in PBS, the cells were mounted in Mowiol containing DABCO. Light microscopy was performed utilizing a Leica TCS SP8 confocal laser-scanning microscope (Leica Microsystems). Except contrast stretching and smoothing, no other image processing was performed.

Cryo-Immunogold Electron Microscopy and Data Analysis. Yeast cells were grown to the early exponential phase (OD_{600} = 0.4 to 0.7) in YPG medium at 30 °C. The cells were fixed with formaldehyde as well as glutaraldehyde, and ultrathin sections (ultra-cryomicrotome [Leica Microsystems] equipped with a diamond knife [Diatome]) were generated according to the Tokuyasu method as detailed elsewhere (9). The pHGFP tag was detected using a

GFP-specific polyclonal serum (Abcam); the primary antibody was detected using Protein A-gold (10 nm; gift of G. Posthuma, Utrecht University, Utrecht, The Netherlands). Following contrast enhancement through uranyl treatment, the samples were imaged with an electron microscope (CM120). Quantification of protein distributions between the CM and the IBM or the OM and the IM (in the case of Tom70-pHGFP) was performed according to established protocols (5, 9, 27). In brief, the distance between a gold particle and the IBM or the OM was manually measured on the respective image. Particles with a distance ≤20 nm from the IBM were assigned to the IBM, whereas particles residing within the mitochondria and with distances >20 nm from the IBM were assigned to the CM. For the outer membrane protein Tom70-pHGFP, gold particles with a distance ≤20 nm from the OM were assigned to the OM, whereas particles residing within the mitochondria and with distances >20 nm from the OM were assigned to the IM.

Purification of the Yeast F_1F_0 ATP Synthase. Cells were harvested at 10,000 × *g* for 5 min at RT. Then, the cell pellet was resuspended in 0.4 M sorbitol, 50 mM KPi, pH 8.0, 5 mM EDTA to a ratio of 1:3 weight per volume. The cells were disrupted twice with a tabletop homogenizer (Constant Systems) at 35 psi. The sample was then centrifuged down at 10,000 × *g* for 5 min to remove the cell debris. The supernatant was centrifuged at 100,000 × *g* with the Ti45 rotor for 80 min at 4 °C. The pellet fraction was then homogenized in a glass vessel (Sartorius; 60 mL) in a buffer containing 20 mM KPO_4, pH 8.0, 100 mM KCl. The sample was centrifuged down at 100,000 rpm at 4 °C for 40 min. The pellet fraction was homogenized again in a buffer with 50 mM KPO_4, pH 8.0, to an appropriate volume. Protein concentration was determined with a BCA assay kit (Thermo Scientific Pierce Protein Assay). The rest of the sample was snap-frozen in liquid nitrogen and kept at −80 °C. Membranes were thawed and solubilized with solubilization buffer, which contained 1% DDM, 50 mM KPO_4, pH 7.9, 200 mM KCl, 20 mM imidazole, pH 7.9, 1 mM EDTA, 1 mM PMSF, 2 mM aminohexanoic acid, and 10% glycerol for 30 min at 4 °C in a beaker under constant stirring. This was followed by a clarifying spin at 52,000 rpm for 1 h 10 min at 4 °C. The supernatant was then transferred to the previously equilibrated Ni-NTA Agarose (Qiagen) beads and let bind for 2 h at 4 °C in a beaker with constant stirring. The washing steps were performed in an Econo chromatography column, 2.5 × 30 cm. The beads were then finally eluted with the same buffer composition as before except for 0.05% DDM and 500 mM imidazole, pH 7.9. The elution fractions were then pooled and concentrated, followed by analysis with Blue Native electrophoresis and silver staining for analysis of proper integrity of the purified F_1F_0 ATP synthase.

Liposome Preparation. One hundred milligrams of soybean asolectin (Type II-S) was resuspended in 10 mL liposome buffer (5 mM MES, 5 mM Tricine, 0.5 mM KCl, 5% sucrose, 10 mM $MgSO_4$, pH 8 with NaOH) by 10 min vortexing. The suspension (10 mg/mL lipids) was frozen in liquid nitrogen and thawed in a water bath at 30 °C and briefly vortexed. This procedure was repeated six times to obtain unilamellar liposomes. Sizing of the liposomes (50 nm or 200 nm) was achieved by passing the liposome suspension 15 times through a polycarbonate filter with the appropriate pore size (Whatman).

Reconstitution of ATP Synthase into Liposomes. Liposomes (220 μL; 10 mg/mL) were mixed with 7.5 μL Na-cholate 20% (final concentration 0.6%) and 25 μL *S. cerevisiae* ATP synthase ∼0.1 mg/mL (final amount ∼10 μg) with or without 1 μL *E. coli* bo_3 oxidase ∼1 mg/mL (final amount ∼1 μg) and incubated at RT for 30 min. Na-cholate was removed by gel filtration, and the liposomes were collected by ultracentrifugation (90 min, 200,000 × *g*, 4 °C).

ATP Synthesis by Acid/Base Transition and Potassium/Valinomycin Potential Determined by a Luciferin/Luciferase Assay. This method is adapted from a previous publication (70). Proteoliposomes (∼1.2 μg proteins) were resuspended in acid buffer (50 mM MES [or other buffer depending of the desired pH_{in}], 5 mM $MgCl_2$, 50 mM NaCl, 0.5 mM KCl, 20% sucrose, pH adjusted to desired value with NaOH). Alternatively, the proteoliposomes were resuspended in liposome buffer and mixed 1:10 with acid buffer, and they were incubated at RT for 1 h. In a 1.5-mL tube placed in a GloMax luminometer (Promega), 450 μL of a basic mixture was pipetted, consisting of base buffer (350 mM Tricine or Hepes or MES [depending on the desired pH_{out}], 5 mM $MgCl_2$, 50 mM NaCl, 100 mM KCl, pH adjusted to desired value with NaOH), 80 μM ADP, 500 μg/mL luciferase reagent of an ATP Bioluminescence Assay Kit HS II, 20 μM valinomycin, and 30 mM sodium phosphate buffer at same pH than the base buffer, with or without 1 μM of the inhibitor CCCP (protonophore). The luminometer baseline measurement (10 data points per second) was started, and the reaction initiated by rapid addition of 50 μL proteoliposomes. After the signal had reached a plateau, 20 nM ATP was added for standardization.

Statistical Analysis. Student's *t* test was used for calculating statistical significance, with a two-tailed distribution with unequal variance. All experiments represent a minimum of three independent experiments, with the bars showing the mean values with ± SD.

Data Availability Statement. Data supporting this manuscript have been uploaded on the Mendeley Dataset public repository (DOI: 10.17632/6vcjtzxgmj) or are presented within this paper and in the accompanying *SI Appendix*.

ACKNOWLEDGMENTS. We thank the members of our groups for stimulating discussions. This work was supported by grants from the Swedish Research council and the Knut och Alice Wallenberg foundation (to M.O. and C.v.B.) and the German Research Foundation-funded SFB1286 (project A5; to S.J.).

1. G. E. Palade, An electron microscope study of the mitochondrial structure. *J. Histochem. Cytochem.* **1**, 188–211 (1953).
2. W. Neupert, Protein import into mitochondria. *Annu. Rev. Biochem.* **66**, 863–917 (1997).
3. M. Schleyer, W. Neupert, Transport of proteins into mitochondria: Translocational intermediates spanning contact sites between outer and inner membranes. *Cell* **43**, 339–350 (1985).
4. A. Chacinska *et al*., Mitochondrial translocation contact sites: Separation of dynamic and stabilizing elements in formation of a TOM-TIM-preprotein supercomplex. *EMBO J.* **22**, 5370–5381 (2003).
5. F. Vogel, C. Bornhövd, W. Neupert, A. S. Reichert, Dynamic subcompartmentalization of the mitochondrial inner membrane. *J. Cell Biol.* **175**, 237–247 (2006).
6. C. A. Wurm, S. Jakobs, Differential protein distributions define two sub-compartments of the mitochondrial inner membrane in yeast. *FEBS Lett.* **580**, 5628–5634 (2006).
7. S. Stoldt *et al*., Spatial orchestration of mitochondrial translation and OXPHOS complex assembly. *Nat. Cell Biol.* **20**, 528–534 (2018).
8. K. M. Davies *et al*., Visualization of ATP synthase dimers in mitochondria by electron cryo-tomography. *J. Vis. Exp.* **14**, 51228 (2014).
9. S. Stoldt *et al*., The inner-mitochondrial distribution of Oxa1 depends on the growth conditions and on the availability of substrates. *Mol. Biol. Cell* **23**, 2292–2301 (2012).
10. T. Brandt *et al*., Changes of mitochondrial ultrastructure and function during ageing in mice and Drosophila. *eLife* **6**, e24662 (2017).
11. L. Scorrano *et al*., A distinct pathway remodels mitochondrial cristae and mobilizes cytochrome c during apoptosis. *Dev. Cell* **2**, 55–67 (2002).
12. W. Junge, Protons, the thylakoid membrane, and the chloroplast ATP synthase. *Ann. N. Y. Acad. Sci.* **574**, 268–286 (1989).
13. C. A. Mannella, M. Marko, P. Penczek, D. Barnard, J. Frank, The internal compartmentation of rat-liver mitochondria: Tomographic study using the high-voltage transmission electron microscope. *Microsc. Res. Tech.* **27**, 278–283 (1994).
14. M. Strauss, G. Hofhaus, R. R. Schröder, W. Kühlbrandt, Dimer ribbons of ATP synthase shape the inner mitochondrial membrane. *EMBO J.* **27**, 1154–1160 (2008).
15. D. A. Cherepanov, B. A. Feniouk, W. Junge, A. Y. Mulkidjanian, Low dielectric permittivity of water at the membrane interface: Effect on the energy coupling mechanism in biological membranes. *Biophys. J.* **85**, 1307–1316 (2003).
16. M. Brändén, T. Sandén, P. Brzezinski, J. Widengren, Localized proton microcircuits at the biological membrane-water interface. *Proc. Natl. Acad. Sci. U.S.A.* **103**, 19766–19770 (2006).
17. E. S. Medvedev, A. A. Stuchebrukhov, Proton diffusion along biological membranes. *J. Phys. Condens. Matter* **23**, 234103 (2011).
18. E. Weichselbaum *et al*., Origin of proton affinity to membrane/water interfaces. *Sci. Rep.* **7**, 4553 (2017).
19. B. Rieger, W. Junge, K. B. Busch, Lateral pH gradient between OXPHOS complex IV and F(0)F(1) ATP-synthase in folded mitochondrial membranes. *Nat. Commun.* **5**, 3103 (2014).
20. G. Miesenböck, D. A. De Angelis, J. E. Rothman, Visualizing secretion and synaptic transmission with pH-sensitive green fluorescent proteins. *Nature* **394**, 192–195 (1998).
21. M. J. Mahon, pHluorin2: An enhanced, ratiometric, pH-sensitive green florescent protein. *Adv. Biosci. Biotechnol.* **2**, 132–137 (2011).
22. C. Janke *et al*., A versatile toolbox for PCR-based tagging of yeast genes: New fluorescent proteins, more markers and promoter substitution cassettes. *Yeast* **21**, 947–962 (2004).
23. S. Horan, I. Bourges, J. W. Taanman, B. Meunier, Analysis of COX2 mutants reveals cytochrome oxidase subassemblies in yeast. *Biochem. J.* **390**, 703–708 (2005).
24. A. M. Hartley *et al*., Structure of yeast cytochrome c oxidase in a supercomplex with cytochrome bc_1. *Nat. Struct. Mol. Biol.* **26**, 78–83 (2019).
25. S. Rathore *et al*., Cryo-EM structure of the yeast respiratory supercomplex. *Nat. Struct. Mol. Biol.* **26**, 50–57 (2019).
26. R. W. Gilkerson, J. M. Selker, R. A. Capaldi, The cristal membrane of mitochondria is the principal site of oxidative phosphorylation. *FEBS Lett.* **546**, 355–358 (2003).

27. I. E. Suppanz, C. A. Wurm, D. Wenzel, S. Jakobs, The m-AAA protease processes cytochrome c peroxidase preferentially at the inner boundary membrane of mitochondria. *Mol. Biol. Cell* **20**, 572–580 (2009).
28. R. Orij, J. Postmus, A. Ter Beek, S. Brul, G. J. Smits, In vivo measurement of cytosolic and mitochondrial pH using a pH-sensitive GFP derivative in *Saccharomyces cerevisiae* reveals a relation between intracellular pH and growth. *Microbiology* **155**, 268–278 (2009).
29. J. Dzbek, B. Korzeniewski, Control over the contribution of the mitochondrial membrane potential (DeltaPsi) and proton gradient (DeltapH) to the protonmotive force (Deltap). In silico studies. *J. Biol. Chem.* **283**, 33232–33239 (2008).
30. E. M. Rubenstein, M. C. Schmidt, The glucose signal and metabolic p[H+]lux. *EMBO J.* **29**, 2473–2474 (2010).
31. S. Ohlmeier, A. J. Kastaniotis, J. K. Hiltunen, U. Bergmann, The yeast mitochondrial proteome, a study of fermentative and respiratory growth. *J. Biol. Chem.* **279**, 3956–3979 (2004).
32. K. M. Davies, C. Anselmi, I. Wittig, J. D. Faraldo-Gómez, W. Kühlbrandt, Structure of the yeast F_1F_o-ATP synthase dimer and its role in shaping the mitochondrial cristae. *Proc. Natl. Acad. Sci. U.S.A.* **109**, 13602–13607 (2012).
33. P. Paumard *et al*., The ATP synthase is involved in generating mitochondrial cristae morphology. *EMBO J.* **21**, 221–230 (2002).
34. M. E. Harner *et al*., An evidence based hypothesis on the existence of two pathways of mitochondrial crista formation. *eLife* **5**, e18853 (2016).
35. T. B. Blum, A. Hahn, T. Meier, K. M. Davies, W. Kühlbrandt, Dimers of mitochondrial ATP synthase induce membrane curvature and self-assemble into rows. *Proc. Natl. Acad. Sci. U.S.A.* **116**, 4250–4255 (2019).
36. M. Zick, R. Rabl, A. S. Reichert, Cristae formation-linking ultrastructure and function of mitochondria. *Biochim. Biophys. Acta* **1793**, 5–19 (2009).
37. I. Arnold, K. Pfeiffer, W. Neupert, R. A. Stuart, H. Schägger, Yeast mitochondrial F_1F_0-ATP synthase exists as a dimer: Identification of three dimer-specific subunits. *EMBO J.* **17**, 7170–7178 (1998).
38. G. M. Boyle, X. Roucou, P. Nagley, R. J. Devenish, M. Prescott, Identification of subunit g of yeast mitochondrial F_1F_0-ATP synthase, a protein required for maximal activity of cytochrome c oxidase. *Eur. J. Biochem.* **262**, 315–323 (1999).
39. S. Saddar, M. K. Dienhart, R. A. Stuart, The F_1F_0-ATP synthase complex influences the assembly state of the cytochrome bc_1-cytochrome oxidase supercomplex and its association with the TIM23 machinery. *J. Biol. Chem.* **283**, 6677–6686 (2008).
40. C. von Ballmoos, A. Wiedenmann, P. Dimroth, Essentials for ATP synthesis by F_1F_0 ATP synthases. *Annu. Rev. Biochem.* **78**, 649–672 (2009).
41. W. Kühlbrandt, Structure and mechanisms of F-type ATP synthases. *Annu. Rev. Biochem.* **88**, 515–549 (2019).
42. W. Junge, N. Nelson, ATP synthase. *Annu. Rev. Biochem.* **84**, 631–657 (2015).
43. J. E. Walker, The ATP synthase: The understood, the uncertain and the unknown. *Biochem. Soc. Trans.* **41**, 1–16 (2013).
44. A. T. Jagendorf, E. Uribe, ATP formation caused by acid-base transition of spinach chloroplasts. *Proc. Natl. Acad. Sci. U.S.A.* **55**, 170–177 (1966).
45. R. M. Fox, R. M. Morgan, A. Markham, Calcium antagonists and Bay K8644 promote depolarization of the rat heart mitochondrial membrane potential. Further evidence for a role in alteration of oxidative metabolism. *Biochem. Pharmacol.* **45**, 1995–2001 (1993).
46. K. Förster *et al*., Proton transport coupled ATP synthesis by the purified yeast H+ -ATP synthase in proteoliposomes. *Biochim. Biophys. Acta* **1797**, 1828–1837 (2010).
47. A. Wiedenmann, P. Dimroth, C. von Ballmoos, Functional asymmetry of the F(0) motor in bacterial ATP synthases. *Mol. Microbiol.* **72**, 479–490 (2009).
48. K. Faelber *et al*., Structure and assembly of the mitochondrial membrane remodelling GTPase Mgm1. *Nature* **571**, 429–433 (2019).
49. A. P. Srivastava *et al*., High-resolution cryo-EM analysis of the yeast ATP synthase in a lipid membrane. *Science* **360**, eaas9699 (2018).
50. A. Hahn, J. Vonck, D. J. Mills, T. Meier, W. Kühlbrandt, Structure, mechanism, and regulation of the chloroplast ATP synthase. *Science* **360**, eaat4318 (2018).
51. H. Guo, T. Suzuki, J. L. Rubinstein, Structure of a bacterial ATP synthase. *eLife* **8**, e43128 (2019).
52. C. von Ballmoos, O. Biner, T. Nilsson, P. Brzezinski, Mimicking respiratory phosphorylation using purified enzymes. *Biochim. Biophys. Acta* **1857**, 321–331 (2016).
53. K. M. Davies, T. B. Blum, W. Kühlbrandt, Conserved in situ arrangement of complex I and III_2 in mitochondrial respiratory chain supercomplexes of mammals, yeast, and plants. *Proc. Natl. Acad. Sci. U.S.A.* **115**, 3024–3029 (2018).
54. M. Pribil, M. Labs, D. Leister, Structure and dynamics of thylakoids in land plants. *J. Exp. Bot.* **65**, 1955–1972 (2014).
55. J. Rosing, E. C. Slater, The value of G degrees for the hydrolysis of ATP. *Biochim. Biophys. Acta* **267**, 275–290 (1972).
56. P. G. Wallace, S. M. Pedler, J. C. Wallace, M. N. Berry, A method for the determination of the cellular phosphorylation potential and glycolytic intermediates in yeast. *Anal. Biochem.* **222**, 404–408 (1994).
57. J. Petersen, K. Förster, P. Turina, P. Gräber, Comparison of the H+/ATP ratios of the H+-ATP synthases from yeast and from chloroplast. *Proc. Natl. Acad. Sci. U.S.A.* **109**, 11150–11155 (2012).
58. M. J. Franklin, W. S. Brusilow, D. J. Woodbury, Determination of proton flux and conductance at pH 6.8 through single F_O sectors from *Escherichia coli*. *Biophys. J.* **87**, 3594–3599 (2004).
59. H. Lill, S. Engelbrecht, G. Schönknecht, W. Junge, The proton channel, CF_0, in thylakoid membranes. Only a low proportion of CF_1-lacking CF_0 is active with a high unit conductance (169 fS). *Eur. J. Biochem.* **160**, 627–634 (1986).
60. B. A. Feniouk *et al*., The proton-driven rotor of ATP synthase: Ohmic conductance (10 fS), and absence of voltage gating. *Biophys. J.* **86**, 4094–4109 (2004).
61. A. A. Guffanti, T. A. Krulwich, ATP synthesis is driven by an imposed delta pH or delta mu H+ but not by an imposed delta pNa+ or delta mu Na+ in alkalophilic Bacillus firmus OF4 at high pH. *J. Biol. Chem.* **263**, 14748–14752 (1988).
62. D. A. Cherepanov, W. Junge, A. Y. Mulkidjanian, Proton transfer dynamics at the membrane/water interface: Dependence on the fixed and mobile pH buffers, on the size and form of membrane particles, and on the interfacial potential barrier. *Biophys. J.* **86**, 665–680 (2004).
63. C. Zhang *et al*., Water at hydrophobic interfaces delays proton surface-to-bulk transfer and provides a pathway for lateral proton diffusion. *Proc. Natl. Acad. Sci. U.S.A.* **109**, 9744–9749 (2012).
64. T. Nilsson *et al*., Lipid-mediated protein-protein interactions modulate respiration-driven ATP synthesis. *Sci. Rep.* **6**, 24113 (2016).
65. Y. Marantz, E. Nachliel, A. Aagaard, P. Brzezinski, M. Gutman, The proton collecting function of the inner surface of cytochrome c oxidase from Rhodobacter sphaeroides. *Proc. Natl. Acad. Sci. U.S.A.* **95**, 8590–8595 (1998).
66. L. N. Ojemyr, H. J. Lee, R. B. Gennis, P. Brzezinski, Functional interactions between membrane-bound transporters and membranes. *Proc. Natl. Acad. Sci. U.S.A.* **107**, 15763–15767 (2010).
67. J. Sjöholm *et al*., The lateral distance between a proton pump and ATP synthase determines the ATP-synthesis rate. *Sci. Rep.* **7**, 2926 (2017).
68. M. Knop *et al*., Epitope tagging of yeast genes using a PCR-based strategy: More tags and improved practical routines. *Yeast* **15**, 963–972 (1999).
69. R. H. Schiestl, R. D. Gietz, High efficiency transformation of intact yeast cells using single stranded nucleic acids as a carrier. *Curr. Genet.* **16**, 339–346 (1989).
70. N. Soga, K. Kinosita, Jr, M. Yoshida, T. Suzuki, Kinetic equivalence of transmembrane pH and electrical potential differences in ATP synthesis. *J. Biol. Chem.* **287**, 9633–9639 (2012).